AGU PUBLICATIONS

JGR

Journal of Geophysical Research: Planets

RESEARCH ARTICLE
10.1002/2013JE004552

Key Points:
- Hot C corona is simulated at the fixed condition within our frameworks
- Background atmosphere greatly impacts the structure of hot C corona
- The estimated global escape rates of hot C is 5.9 x 1023 s-1

Correspondence to:
Y. Lee,
yunilee@umich.edu

Citation:
Lee, Y., M. R. Combi, V. Tenishev, and S. W. Bougher (2014), Hot carbon corona in Mars' upper thermosphere and exosphere: 1. Mechanisms and structure of the hot corona for low solar activity at equinox, *J. Geophys. Res. Planets*, *119*, 905–924, doi:10.1002/2013JE004552.

Received 8 OCT 2013
Accepted 31 MAR 2014
Accepted article online 4 APR 2014
Published online 2 MAY 2014

Hot carbon corona in Mars' upper thermosphere and exosphere: 1. Mechanisms and structure of the hot corona for low solar activity at equinox

Yuni Lee[1], Michael R. Combi[1], Valeriy Tenishev[1], and Stephen W. Bougher[1]

[1]Department of Atmospheric, Oceanic and Space Sciences, University of Michigan, Ann Arbor, Michigan, USA

Abstract Two important source reactions for hot atomic carbon on Mars are photodissociation of CO and dissociative recombination of CO^+; both reactions are highly sensitive to solar activity and occur mostly deep in the dayside thermosphere. The production of energetic particles results in the formation of hot coronae that are made up of neutral atoms including hot carbon. Some of these atoms are on ballistic trajectories and return to the thermosphere, and others escape. Understanding the physics in this region requires modeling that captures the complicated dynamics of hot atoms in 3-D. This study evaluates the carbon atom inventory by investigating the production and distribution of energetic carbon atoms using the full 3-D atmospheric input. The methodology and details of the hot atomic carbon model calculation are given, and the calculated total global escape of hot carbon from the assumed dominant photochemical processes at a fixed condition, equinox ($L_s = 180°$), and low solar activity ($F10.7 = 70$ at Earth) are presented. To investigate the dynamics of these energetic neutral atoms, we have coupled a self-consistent 3-D global kinetic model, the Adaptive Mesh Particle Simulator, with a 3-D thermosphere/ionosphere model, the Mars Thermosphere General Circulation Model to provide a self-consistent global description of the hot carbon corona in the upper thermosphere and exosphere. The spatial distributions of density and temperature and atmospheric loss are simulated for the case considered.

1. Introduction

Exploring the physical processes that affect the volatiles in Martian atmosphere will help provide a better understanding of the water and CO_2 inventories on Mars [e.g., *Carr*, 1986; *Pepin*, 1994; *Jakosky and Jones*, 1997; *McElroy*, 1972]. Throughout the Martian history, the loss mechanisms and the escape rates of Martian atmosphere have changed [*Chassefiére et al*., 2007; *Luhmann*, 1992; *Melosh and Vickery*, 1989]. Observations from spacecraft and analyses of Martian geomorphology suggest that the early Martian atmosphere was much warmer, wetter, and abundant in water and CO_2, which was substantially different from the current atmospheric condition [e.g., *Chassefiére et al*., 2007; *Jakosky*, 1991]. The deficiency of water and CO_2 in the current atmosphere raises questions as to the processes that led to the loss of volatiles and their subsequent fate. Among several possible processes, escape of heavy neutral species by nonthermal mechanisms is posited as a significant factor in the loss on the basis of the current volatile content. Heavy species, such as atomic O and C, can escape through these nonthermal mechanisms, resulting in the formation of hot coronae in the upper atmosphere of Mars. The hot oxygen corona has been observed by the ALICE instrument onboard Rosetta spacecraft during a swingby for gravity assist of Mars [*Feldman et al*., 2011]. The detected Oxygen I (OI) (1304 nm) brightness from limb scans has been compared with the estimated brightness from our model simulation [*Lee et al*., 2012, Y. Lee et al., Hot carbon corona in Mars' upper thermosphere and exosphere: 2. Solar cycle and seasonal variability, *Journal of Geophysical Research*, manuscript in final preparation, 2014]. This observed hot corona shows that hot neutral species play an important role in constructing the current Martian upper atmosphere and exosphere.

CO_2 is the major neutral species in the thermosphere. Its inventory at Mars is constrained by either the escape of carbon as an atom or molecule, such as CO_2, CO, or C, or C-containing ions [*Fox and Hać*, 1999], or the formation of carbonate mineral deposits to the crust by chemical interactions [*Jakosky*, 1991]. Among a number of escape mechanisms, only nonthermal processes can induce the escape of a carbon atom with energy above the escape energy of about 1.48 eV. A carbon atom is considered to be "hot carbon" when the excessive energy from the source mechanisms is added to a nascent carbon atom. Depending on the

©2014. American Geophysical Union. All Rights Reserved.

availability of enough energy to escape, the hot carbon in the corona may escape to space or fall back to the atmosphere by gravitational attraction after traveling along its ballistic trajectory.

A number of numerical approaches have been carried out to estimate the current global escape rate of hot heavy neutral species, in particular, O [*Cipriani et al*., 2007; *Fox*, 1997; *Fox and Hać*, 2009; *Hodges*, 2000, 2002; *Kim et al*., 1998; *Valeille et al*., 2009a, 2009b, 2010a; *Yagi et al*., 2012], C [*Cipriani et al*., 2007; *Fox*, 2004; *Fox and Bakalian*, 2001; *Fox and Hać*, 1999; *Nagy et al*., 2001], and N [*Bakalian*, 2006; *Fox*, 1993; *Fox and Hać*, 1997], which are important for understanding the inventory of water, CO_2, and N_2 in an evolutionary aspect. *Fox and Hać* [1999] used 1-D (spherical) Monte Carlo calculations to investigate the altitude-dependent velocity distributions of hot C produced from dissociative recombination of CO^+ only. They used a fixed exobase for each solar activity case and studied the effect of using different upper atmosphere conditions—"eroded" and "noneroded" ionospheres. *Fox and Bakalian* [2001] calculated the escape fluxes by using the "exobase approximation" for various photochemical mechanisms and found that photodissociation of CO and dissociative recombination of CO^+ are the dominant source mechanisms of hot C. *Nagy et al*. [2001] used the two-stream approach to describe the hot C corona, which was also a one-dimensional study that adopted the production rates from *Fox and Hać* [1999]. Interestingly, *Fox* [2004] included dissociative recombination reaction of CO_2^+ in their study and reported that the second most dominant source of hot C is electron impact dissociation of CO. *Cipriani et al*. [2007] used a 1-D Monte Carlo test particle approach with the same thermospheric models as those of previous hot C studies. They reported a range of hot atom and molecule production and escape rates in the Martian upper atmosphere. Their reported escape rates of the hot C from dissociative recombination of CO^+ are somewhat lower than previously published values.

Hot carbon exospheric models have been significantly improved and investigated extensively the source mechanisms of hot carbon. However, the approaches so far to study the hot carbon corona in the atmosphere of Mars have been limited to one-dimensional numerical schemes and/or thermospheric inputs for fixed orbital positions. The processes that characterize the Martian exosphere occur deep within the thermosphere and ionosphere, where the complicated local variations occur as an inevitable result of the pure 3-D planetary influences. For example, asymmetries in thermosphere/ionosphere, planetary rotation, winter polar warming, and interhemispheric dynamics [e.g., *Bougher et al*., 2000, 2004, 2006, 2008, 2009, S. W. Bougher et al., Mars Global Ionosphere Thermosphere Model (M-GITM): Solar cycle, seasonal, and diurnal variations of the upper atmosphere, *Journal of Geophysical Research*, manuscript in final preparation, 2014] have been successfully described. The upward propagating gravity waves and tides from the lower atmosphere modify the energy and momentum in the upper atmosphere, resulting in the changes in the atmospheric circulation and horizontal distributions of atmospheric constituents. These effects of dynamics have been inherently neglected in the past 1-D and 2-D models. Consequently, they may have over/underestimated the overall structure of the upper Martian atmosphere and hot corona. In order to overcome these limitations in previous models, a global kinetic model with a self-consistent thermosphere-ionosphere-exosphere description is required.

A full 3-D study of the exosphere presented here provides a detailed description of the Martian upper atmosphere and a better understanding of the Martian hot carbon corona. The 3-D Mars Thermosphere General Circulation Model (MTGCM) [*Bougher et al*., 2006, 2009] provides all the necessary background thermospheric/ionospheric parameters as inputs to our 3-D Adaptive Mesh Particle Simulator (AMPS) code [*Tenishev et al*., 2008, 2013]. The combination of the 3-D thermosphere/ionosphere (MTGCM) and 3-D exosphere/kinetic model (AMPS) frameworks provides a self-consistent evaluation of the neutral hot carbon corona. Utilizing the same coupled framework, the recent studies by *Valeille et al*. [2009a, 2009b, 2010a, 2010b] have successfully addressed the global description of the hot oxygen corona both in current and evolutionary aspects.

In this work, our global approach of modeling the Martian hot neutral corona is presented using one-way coupling between the MTGCM and AMPS models. The main assumptions and methods are discussed in section 2. The mechanisms for production of hot carbon in the Martian upper atmosphere are presented in section 3, along with the 3-D descriptions of the Martian thermosphere and ionosphere in section 4. The detailed study and comparisons of the simulated Martian hot carbon corona are presented in section 5, and we discuss conclusions in section 6. As for the purpose of this work, our coupled framework in this paper considers the fixed Martian seasonal and solar cycle conditions, equinox ($L_s = 180°$) and low solar activity ($F10.7 = 70$ at Earth). The variability of seasons and solar cycle on the hot carbon corona is investigated in depth in Paper II (Y. Lee et al., manuscript in final preparation, 2014).

©2014. American Geophysical Union. All Rights Reserved.

2. Models

2.1. AMPS

2.1.1. Numerical Approach and Assumptions

Unlike the Earth's atmosphere, the Martian atmosphere is tenuous and has a low surface pressure of about 6 mbar; this is likely due to both to its lower gravity (small size and mass) and the absence of a permanent magnetic field since an early epoch of the solar system [*Acuna et al*., 1998; *Smith et al*., 1965]. Especially, in the upper atmosphere, the exponential decrease of density with increasing altitude reaches a point where energy transitions are no longer dominated by collisions, deviating from local thermodynamic equilibrium (LTE), and so numerical modeling of this region is challenging [*Combi*, 1996]. This region is a rarefied multispecies gas flow regime under nonequilibrium conditions, which can be appropriately described with the Boltzmann collision integral equation,

$$\frac{\partial f_s}{\partial t} + \boldsymbol{v_s} \cdot \nabla f_s + \boldsymbol{a_s} \cdot \nabla_{\boldsymbol{v}} f_s = \frac{\delta f_s}{\delta t} = \sum_p \int_\infty \int_0^{4\pi} \left[f_s^* f_p^* - f_s f_p \right] g_{sp} \sigma_{sp} \mathrm{d}\Omega \mathrm{d}\boldsymbol{v_p},$$

where $f_s \equiv f_s(t, \boldsymbol{x}, \boldsymbol{v_s})$ denotes the phase space distribution function of species of type "*s*," the asterisk represents the postcollision state, *x* is the spatial coordinate, $\boldsymbol{v_s}$ is the velocity, $\boldsymbol{a_s}$ is the acceleration, Ω is the solid angle, σ_{sp} is the total collision cross section between species *s* and *p*, and $g_{sp} \equiv |v_s - v_p|$. The Boltzmann equation is an integro-differential equation, which contains the collisional integral and describes the evolution of the distribution function of macroscopic characteristics.

The collisional integration usually makes solving the Boltzmann equation intractable either analytically or numerically; thus, a kinetic particle approach that does not require the formulation of integro-differential equation is needed. The standard method for solving the Boltzmann equation in cases like this has been developed using the Direct Simulation Monte Carlo (DSMC) [*Bird*, 1994] method. As a key feature, the DSMC method separates the translational motion of species from the intermolecular interaction, allowing a description of a much wider relaxation scheme than the Boltzmann equation does. During the relaxation stage, the velocity coordinates of collision partners from the same cell can be changed due to a chosen probabilistic relaxation model.

The Monte Carlo method allows development of the numerical algorithm that is based on a simulation of the relaxation process of the distribution function in a rarefied gas. The Monte Carlo scheme is generally described by a Markov chain, a discrete-time process, which describes that the future behavior only depends on the present. As a continuous-time version, the Markov process [*Hochstim*, 1969] is used to describe the evolution of the distribution function, $f(v, t)$, which is represented in the integral from,

$$f(\boldsymbol{v}, t + \Delta t) = \int f(\boldsymbol{v} - \Delta \boldsymbol{v}, t) P(\boldsymbol{v} - \Delta \boldsymbol{v}, \Delta \boldsymbol{v}) \mathrm{d}(\Delta \boldsymbol{v}),$$

together with the normalization,

$$\int P(\boldsymbol{v}, \Delta \boldsymbol{v}) \mathrm{d}(\Delta \boldsymbol{v}) = 1.$$

The function evolves as the probability, $P(\boldsymbol{v}, \Delta \boldsymbol{v})$, for the velocity of *v* of a particle at time *t* converges to the velocity of $\boldsymbol{v} + \Delta \boldsymbol{v}$ at time $t + \Delta t$, without being affected by the previous history.

This Monte Carlo simulation computes an averaged value of macroscopic functions, including density, velocity, and flux, over defined regions of phase space using the standard kinetic theory definitions. Since a probabilistic relaxation scheme is based on collisions, the total collision frequency, *v*, is a key quantity. From the Boltzmann collision integral, *v* can be defined as,

$$v = \frac{n}{N} \sum_{i<j} \int \omega \left(\boldsymbol{v_i} \boldsymbol{v_j} \rightarrow \boldsymbol{v_i'} \boldsymbol{v_j'} \right) \mathrm{d}^3 \boldsymbol{v_i} \mathrm{d}^3 \boldsymbol{v_j} = \frac{n}{N} \sum_{i<j} \sigma_t \left(g_{ij} \right) g_{ij},$$

where $\sigma_t(g_{ij})$ is the total collision cross section, g_{ij} is the relative speed between species *i* and *j*, and ω is the total momentum cross section. The summation is performed over $N(N-1)/2$ possible pairs for collisions. The post collision velocities are computed in accordance with the laws of conservation of mass, momentum, and energy in every intermolecular interaction.

Using the DSMC method allows incorporation of complex physical processes without a significant complication of the numerical procedure. The DSMC approach has been used in other applications, such as

©2014. American Geophysical Union. All Rights Reserved.

the investigations of the cometary coma and the upper atmospheres of other planets; examples are found in *Combi* [1996], *Crifo et al*. [2005], *Markelov et al*. [2006], and *Tenishev et al*. [2008, 2011, 2013].

The University of Michigan Adaptive Mesh Particle Simulator (AMPS) code [*Tenishev et al*., 2008, 2013] was first coded for solving the Boltzmann equation of the gas flow in the coma of a comet [*Tenishev et al*., 2008]. The AMPS is developed within the frame of the DSMC method, which employs a stochastic solver for both the linear and nonlinear Boltzmann equations. As a standard numerical method today, this DSMC method can represent the collisional dynamics of a finite number of model particles in a rarefied gas flow regime, such as Mars upper atmosphere. In place of solving the intractable Boltzmann equation, the AMPS simulates the ensemble of model particles and captures the physics of the distribution of gas species in tenuous upper atmospheres, where the transitions from a local thermodynamic equilibrium (LTE) region to a non-LTE region occur. The cell size of our computational domain varies by the lower and upper limit of the cell sizes, which are predetermined in the initialization process.

Utilizing the technique of the Adaptive Mesh Refinement, which will be discussed in the next section, the cell size is the smallest only where the important production of hot particles and interaction between nascent hot particles and background atmosphere take place. The nominal cell size is about 80 km at the bottom of the computational domain, and the maximum cell size is determined by the designated upper boundary of the domain. In general, our simulation scheme does not require the limitation of the characteristic size of computational cells, since the simulation is rather closely related to the spatial distribution, gradient, and collision frequencies of the local background densities. The cell size matters only for averaging the macroscopic parameters and can be as large as 80 km at the bottom of our domain without affecting the overall computation. For the purpose of sampling the macroscopic parameters, we discuss a special treatment that we applied on our mesh in the next section. The typical size of the domain can be set as small as about 2–3 Mars radii, which allows the reduction of computational time and resources to compute escape rates of neutral particles without overestimating the escapes. The local time step is determined by the ratio between the smallest characteristic cell size and the upper limit of the hot carbon speed. Typically, the simulation runs fast enough with the local time step of about 2 s. This local time step is set large enough for the code to recognize a modeling particle in the same cell for at least a few iterations during the simulation.

2.1.2. Three-Dimensional Adaptive Mesh Refinement and Auxiliary Mesh

Modeling a large number of particles with realistic reactions and interactions in time- and region-dependent gas systems requires high computational cost. Prior to this work, the unstructured mesh of tetrahedral cells [*Valeille et al*., 2009a, 2009b, 2010a, 2010b] method determined the local values at the points on the mesh, which is generated at the beginning of the simulation with fixed spacing. This approach had the advantage of a fine radial resolution (e.g., about one half to one third of the local scale height in the transitional domain) capturing steep density gradients with altitude. However, to cover the critical details in the atmosphere, simulation on this mesh demanded too much computing time and resources, and even with this high resolution, the computation on the mesh could not guarantee satisfactory accuracy over the whole domain.

Our model methodology now utilizes the technique of the Adaptive Mesh Refinement [*Berger and Colella*, 1989], which is computationally efficient for realistic simulations of the atmosphere of Mars. This current mesh algorithm is capable of an appropriate description of the regions in the atmosphere with important features by minimizing the use of computational resources. Since a finer mesh is placed over a base coarse mesh covering the whole domain, the local enhancement of mesh resolution effectively handles the regions of interest with the local time step and cell size. At present, our use of this mesh drastically reduced the use of the computation time and resources and increased the accuracy of our simulation.

The physical situation that needs to be modeled involves sharp density gradients in the lower altitude region (about 80–200 km). The macroscopic parameters, such as production rate and density, are difficult to sample and visualize in these regions since the cell is not small enough to capture the rate of change. For example, the density of CO^+ has an abrupt inflection point at around 140 km altitude and an exponential decrease after its peak density at an altitude of about 210 km (for the low solar activity case). The production rate of hot oxygen has a sharp radial gradient deep in the thermosphere. To sample these local features accurately, one can increase the resolution of the mesh in the lower altitude region. However, it is too costly in

©2014. American Geophysical Union. All Rights Reserved.

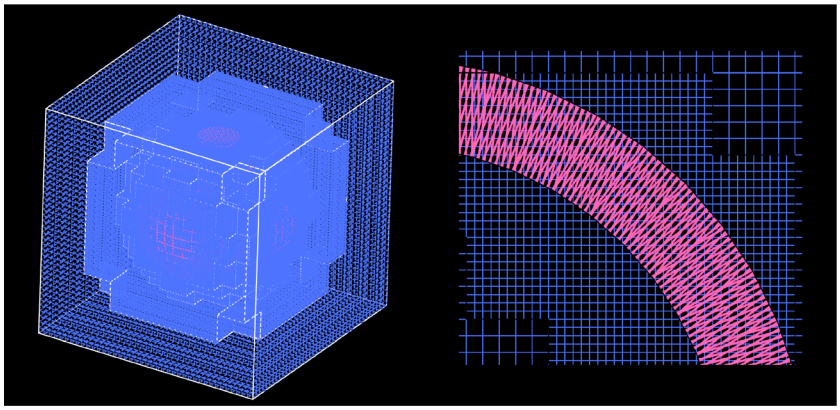

Figure 1. (a) The 3-D computational domain (cubic cells, blue) and overlaid spherical auxiliary mesh (pink). (b) A sectional view of the region of interest.

computation to increase the resolution of our cubic cell mesh just for a sampling purpose. The other solution, which we have applied in our mesh, is that we overlay an auxiliary mesh, a spherical coordinate mesh, on our Cartesian coordinate mesh (Figure 1). In 3-D, the overlapping mesh is like a shallow sphere centered at the origin of our simulation. This auxiliary mesh resembles our previous mesh [*Valeille et al*., 2009a, 2009b, 2010a, 2010b], but it is a simple spherical mesh that permits us to take the advantage of the fine radial resolution when we need to sample macroscopic parameters from our computational domain. The thickness of the shell, which can be adjusted manually, is the range of the region of interest. This auxiliary mesh is used only for sampling purpose and not a part of our computational domain.

2.2. MTGCM

The MTGCM is a 3-D finite difference primitive equation model that self-consistently solves for time-dependent neutral temperatures, neutral ion densities, and three-component neutral winds over the globe [*Bougher et al*., 1999, 2000, 2002, 2004, 2006, 2009]. Above a 1.32 μbar level (33 pressure level), corresponding to an altitude range of about 70–300 km for solar maximum conditions, prognostic equation fields for the major neutral species (CO_2, CO, N_2, and O), selected minor neutral species (Ar, He, and O_2), and photochemically produced ions (e.g., O_2^+, CO_2^+, O^+, CO^+, and NO^+ below 180–200 km) are simulated with a 5° latitude and 5° longitude grid resolution. The MTGCM has log-pressure vertical coordinate with 0.5 scale height spacing. The important feedback of simulated O atoms upon CO_2 cooling rates is captured by implementing a fast nonlocal thermodynamic equilibrium (non-LTE) 15 μm cooling scheme with corresponding near-IR heating rates [e.g., *Bougher et al*., 2006; *López-Valverde et al*., 1998]. The *F*10.7 index (solar EUV/UV flux variation), the heliocentric distance, and solar declination, which are key parameters for Martian seasons and solar cycle variations, can be adjusted to customize MTGCM cases for different purposes of study.

The MTGCM is currently an upward coupling model that is driven from below by the NASA Ames Mars General Circulation Model (MGCM) code [e.g., *Haberle et al*., 1999] at the 1.32 μbar level. At this pressure level, key variables, such as zonal and meridional winds, temperatures, and geopotential heights, are passed upward (only) from the MGCM crossing the lower boundary of the MTGCM on a 2 min time step. This one-way coupling provides a realistic description of the Martian lower atmosphere to the MTGCM regime by including the continuous effects of upward propagating migrating and nonmigrating tides and the seasonal effects of the expansion and contraction of the lower atmosphere. Various applications of this coupled MGCM-MTGCM framework have successfully (1) reproduced observed thermospheric polar warming features [*Bougher et al*., 2006, 2008], (2) derived exospheric temperatures [*Bougher et al*., 2000, 2009, S. W. Bougher et al., manuscript in final preparation, 2014], (3) measured nightside mesopause temperatures [*McDunn et al*., 2010], and (4) measured longitude variations of the thermosphere and ionosphere density structure [e.g., *Bougher et al*., 2004]. The MTGCM can, thus, provide an appropriate simulation of the Martian upper atmosphere structure.

©2014. American Geophysical Union. All Rights Reserved.

2.3. Coupling and Framework

In this work, the 3-D MTGCM simulates the exact Martian seasonal and solar cycle conditions considered in this paper, utilizing equinox ($L_s = 180°$) and low solar activity ($F10.7 = 70$ at Earth) parameters. The densities of thermosphere-ionosphere species (O, CO, CO_2, CO^+, O_2^+, and e^-), temperatures (T_n, T_i, and T_e), and three-component neutral winds (zonal, meridional, and vertical winds) are compiled in the MTGCM in the frame of the AMPS to be used as the necessary parameters for the production of hot carbon and background atmosphere. As our atmospheric input, these thermosphere/ionosphere parameters are precalculated by the MTGCM from 135 km to 200 km altitude and supplied to the AMPS, achieving one-way coupling between the MTGCM and AMPS. Above our input boundary (i.e., 200 km altitude), the AMPS code extrapolates the density profiles using the local density scale height. It is a realistic and safe assumption to use this extrapolation scheme to estimate the density beyond the upper boundary of our atmospheric input since the important production of hot carbon and gradients occur within our input domain. The contribution from the atmosphere below the lower boundary of our input domain is assumed to be negligible to the result. The exception is the dissociative recombination of CO^+, where CO^+ density could not be extrapolated as is done for the densities of other background species. However, the computed peak production rate of the dissociative recombination of CO^+ is still located below an altitude of 200 km because the reaction is also dependent on the electron temperature and electron density, which vary significantly with altitude. The detailed description of the special treatment for CO^+ density is discussed in section 4. Our extrapolation scheme was used in the previous works by *Valeille et al*. [2009a, 2009b, 2010a, 2010b]. As mentioned in those previous works, our background atmosphere, which consists of the MTGCM input and the extrapolation, is in good agreement with the observations from the Viking Landers [*Hanson et al*., 1977; *Nier and McElroy*, 1977], Mars Global Surveyor (MGS) [*Withers et al*., 2008; *Withers and Mendillo*, 2005], and Mars Express [*Morgan et al*., 2008].

The AMPS code considers a particle in the domain to be a hot atom when it satisfies the local velocity criterion, $V_{\text{model particle}} > V_{\text{threshold}}$. For computational purposes, this work sets $V_{\text{threshold}}$ to either twice the local thermal speed or the local escape speed. As noted by *Valeille et al*. [2010a], setting $V_{\text{threshold}}$ to twice the local thermal speed results in the hot population that are less than the hottest 1% of the Maxwellian distribution of thermospheric population. This setting is validated by *Valeille et al*. [2010a] as a best estimated $V_{\text{threshold}}$, ensuring a clear separation between hot and cold population. Separately, we can set $V_{\text{threshold}}$ to the local escape speed for the purpose of reducing resources and computational time without underestimating the escaping hot atoms.

The AMPS is a DSMC model that runs in a test particle Monte Carlo mode for the Martian hot atomic corona calculations. The AMPS has been used in full DSMC mode for the simulation of cometary coma [e.g., *Tenishev et al*., 2008]. The motion of each hot particle is influenced by the gravitational field of Mars and affected by the collisions with background species on its way to escape to space or to become part of the cold population (i.e., thermospheric population). The only collision case that we consider in our simulation is the collisions between hot carbon and background species. The collisions between hot carbon atoms can be also possible. However, due to relatively low density of hot carbon, the collision frequency of C_{hot}-C_{hot} is much smaller than that of C_{hot}-background species (O and CO_2). The C_{hot}-O_{cold} collision frequency is on the order of 10^{-3} s^{-1} near an altitude of 200 km, and the upper limit of the C_{hot}-C_{hot} collision frequency is estimated to be on the order of 10^{-8} s^{-1}. Thus, we safely disregard the collisions between hot carbon atoms since its effect is negligible.

We assume that all scatterings occurring between a nascent hot carbon and background species in our simulation are elastic hard sphere collisions. We approximate both C_{hot}-O_{cold} and C_{hot}-$CO_{2,\,cold}$ collision cross sections to be 3×10^{-15} cm^2. Current other studies might suggest different cross sections and angular scattering models, such as an integrated cross section (i.e., a forward scattering collision scheme). If a considerable reassessment is required for collisions, we expect the overall result to reflect the difference. For example, different collision frequencies resulting from using reassessed scattering models can affect the changes in the velocity distribution of nascent hot carbon and the total global escape rates. As has been done in other studies [e.g., *Fox and Hać*, 2009], the effects of using different approximations for collisions on hot carbon escape should be investigated in the future and can easily be incorporated into the AMPS without noticeable loss in computational efficiency.

©2014. American Geophysical Union. All Rights Reserved.

In our coupled MTGCM and AMPS framework, the exobase is not designated as a fixed altitude that separates the collision (thermosphere) and collisionless (exosphere) regimes. Instead, this study considers the full transitional domain, which extends from the altitude where a hot particle produced in this region has a high probability to be thermalized to where the collision frequency is very low. Our assumption is that this transitional domain exists from 135 km to 300 km altitude and has been confirmed by *Valeille et al*. [2010a] by a range of different test runs for hot oxygen production. In this region, the collision frequency that the AMPS computes during the simulation decreases by an order of magnitude, which is from about a few 10^{-1} s^{-1} to 10^{-2} s^{-1}.

3. Hot Carbon Escape by Photochemical Mechanisms

Carbon atoms are produced with enough energy to escape in the lower exosphere (around 200 km), through a number of photochemical mechanisms, such as photoelectron impact dissociation of CO, photodissociative ionization of CO, and photoelectron impact dissociative ionization of CO^+. Among these mechanisms, many of the previous studies have found that photodissociation of CO and dissociative recombination of CO^+ are the two important mechanisms that produce a suprathermal carbon with energy in excess of the escape energy of a carbon atom. *Nagy et al*. [2001] also considered the collision of hot oxygen with cold, thermal carbon as a potentially important source, but it was found to have negligible effect at Mars. Various sources were investigated by *Fox* [2004] using the solar fluxes that were characterized with enhanced soft X-ray and different EUV fluxes. *Fox* [2004] concluded that the most important source of escaping carbon is predicted to be photodissociation of CO, followed by electron impact dissociation of CO and dissociative recombination of CO^+. While the main sources of hot carbon are not firmly agreed upon, this work assumes that only photodissociation of CO and dissociative recombination of CO^+ are the two major sources of hot carbon in the Martian thermosphere, based on the majority of the previous studies [*Cipriani et al*., 2007; *Fox and Bakalian*, 2001; *Fox and Hać*, 1999; *Nagy et al*., 2001]. Sputtering of the upper thermosphere by energetic pickup ions [*Leblanc and Johnson*, 2002] is likely to be an important loss mechanism for atomic carbon but including this in an equivalent full 3-D description is beyond the scope of this study.

The most prominent current source of escaping hot carbon is expected to be photodissociation of CO, which is highly sensitive to solar UV fluxes. We have assumed that, in the reaction,

$$CO\left(X^1\Sigma^+\right) + h\nu \rightarrow C\left(^3P\right) + O\left(^3P\right),$$

the produced C and O are both in their ground state with the excess energies [*Huebner et al*., 1992] distributed in accordance with the laws of conservation of momentum and energy. Studies of this reaction [e.g., *Krupenie and Weissman*, 1965; *Fox and Black*, 1989; *Torr et al*., 1979] have shown that the threshold for the dissociation of $CO(X^1\Sigma^+)$ to the ground states of C and O is at $\lambda = 1117.8$ Å. The dissociation occurs between $\lambda = 885$ Å and this threshold by line absorption. We have adopted the photodissociation frequencies from *Fox and Black* [1989], which are $4.4 \times 10^{-7} s^{-1}$ and $1.21 \times 10^{-6} s^{-1}$ for the low and high solar activity cases, respectively (scaled to 1 AU heliocentric distance). These frequencies are scaled to the Martian heliocentric distance for $L_s = 180°$. The attenuation of solar flux by the atmosphere is not considered in this work since the photoabsorption cross sections for CO and CO_2 are about 2 orders of magnitude smaller than the collision cross section between a nascent hot carbon and background species ($\sigma_{photoabsorption} \sim 10^{-17}$ cm^2 [*Torr et al*., 1979] for both CO and CO_2; $\sigma_{collision} \sim 10^{-15}$ cm^2). This implies that the altitude where the attenuation is important would be at lower altitudes where the most of nascent hot carbon atoms are thermalized and have substantially small probability to escape.

The dissociative recombination of CO^+ results in a number of energetic channels,

$$CO^+ + e \rightarrow C\left(^3P\right) + O\left(^3P\right) + 2.90 \text{ eV [C1]},$$
$$CO^+ + e \rightarrow C\left(^1D\right) + O\left(^3P\right) + 1.64 \text{ eV [C2]},$$
$$CO^+ + e \rightarrow C\left(^3P\right) + O\left(^1D\right) + 0.94 \text{ eV [C3]},$$
$$CO^+ + e \rightarrow C\left(^1S\right) + O\left(^3P\right) + 0.22 \text{ eV [C4]},$$
$$CO^+ + e \rightarrow C\left(^1D\right) + O\left(^1D\right) - 0.33 \text{ eV [C5]}.$$

©2014. American Geophysical Union. All Rights Reserved.

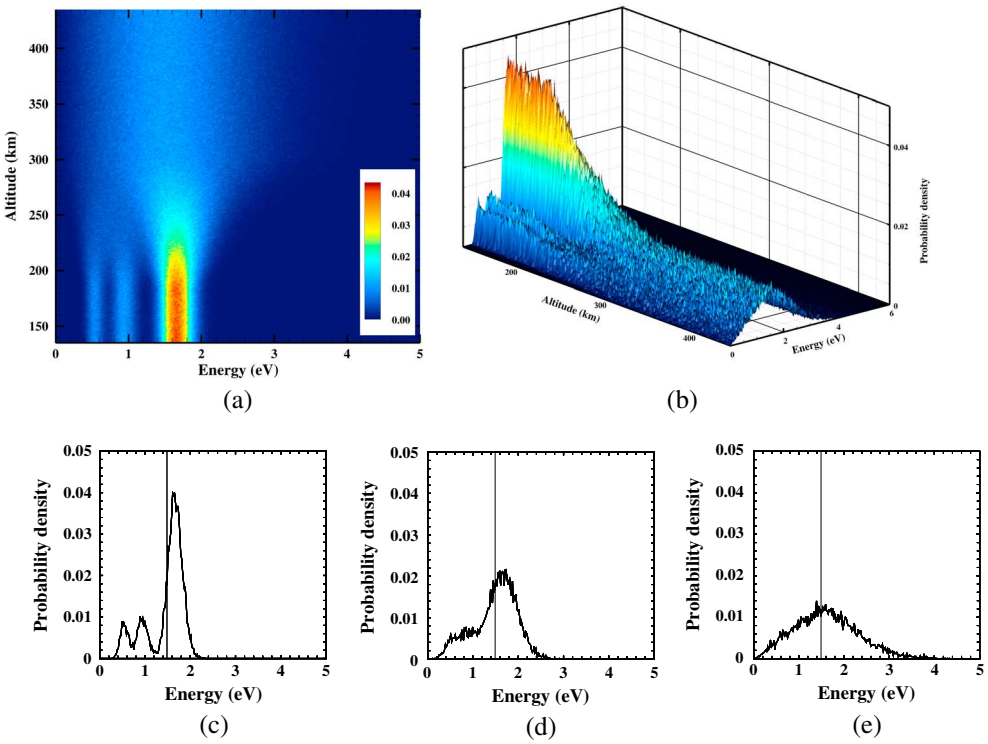

Figure 2. Energy distribution of the nascent hot C from dissociative recombination of CO^+ in (a) 2-D (the contour shows the probability density), (b) 3-D, and 1-D at altitudes of (c) 190 km, (d) 240 km, and (e) 300 km. The vertical line in 1-D plots indicates the escape energy of hot C (~1.48 eV).

The energy released from the reaction depends on the exothermicity of the involved channel. The corresponding branching ratios for the channels have been measured by *Rosén et al.* [1998] at 0 eV relative energy between the CO^+ and the electron, which are 0.761, 0.145, 0.094, and 0.0, respectively, from C1 to C4, with C5 being endothermic. The rate coefficient, which is dependent on electron temperature (T_e),

$$\alpha(T_e) = 2.75 \times 10^{-7}\left(\frac{300}{T_e}\right)^{0.55} \text{cm}^3\ \text{s}^{-1},$$

is adopted also from the measurement by *Rosén et al.* [1998].

The energy distributions (velocity distribution) of nascent hot carbon atoms produced by dissociative recombination of CO^+ are shown for different altitudes in Figure 2. Figures 2a and 2b visualize the changes in the structure of the energy distribution as a function of altitude. The peaks in Figures 2c–2e correspond to the [C1], [C2], and [C3] channels in dissociative recombination of CO^+. The vertical line indicates the escape energy, ~1.48 eV, of a hot carbon atom. CO^+ density in our ionospheric description always peaks above ~200 km where the electron density decreases exponentially. The computed production rate peaks in the altitude region between 150 km and 180 km and decreases by about an order of magnitude near an altitude of 200 km. Because of the ionospheric peak height of CO^+ density, the production of hot carbon is assumed to be still important in vicinity of an altitude of 200 km. Ion temperature increases as altitude increases, which results in the broadening of the peak as shown in Figures 2c–2e. As the probability density for the three available channels decreases with increasing altitude, the peaks are less distinctive and the average energy becomes larger.

4. Characterization of the Sources of Hot Carbon

4.1. Thermosphere/Ionosphere

A strong coupling between the Mars' lower and upper atmosphere has been confirmed by analysis of the aerobraking data from the Mars Global Surveyor (MGS) and Mars 2001 Odyssey Accelerometer, which

©2014. American Geophysical Union. All Rights Reserved.

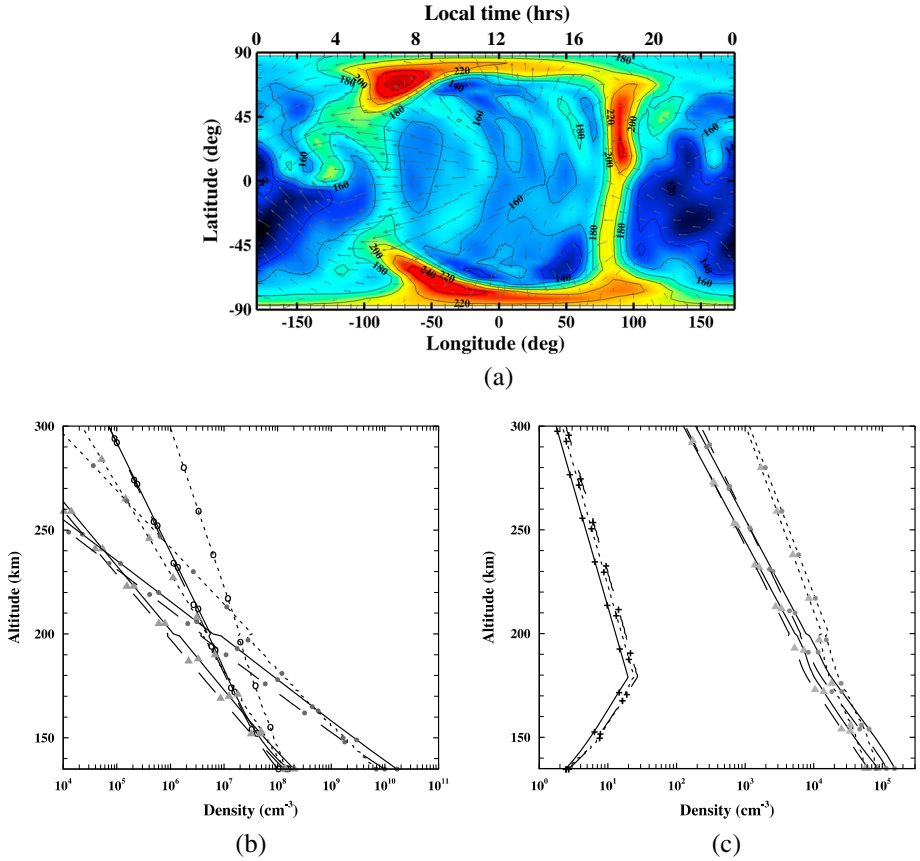

Figure 3. (a) Neutral temperatures (T_n) near 200 km and density profiles of (b) neutral and (c) ion background species for three different SZA along the equatorial east (0°, solid; 60°, dashed; 80°, dotted) for the low solar and equinox case. Global wind magnitudes and directions are indicated as grey arrows. The highest temperature is ~270–280 K and shown in dark red. The contour shows the temperatures in units of K. In the profiles: CO (triangle), O (empty circle), CO_2 (filled circle), CO^+ (plus sign), O_2^+ (triangle), and electron (filled circle).

includes seasonal and dust-driven inflation/contraction, migrating/nonmigrating tidal forcing and interhemispheric circulation [*Bell et al*., 2007; *Bougher et al*., 1999, 2004, 2006; *Forbes et al*., 2002; *Forget et al*., 2009; *Keating et al*., 2003; *Wilson*, 2002; *Withers et al*., 2003]. Several physical processes also drive the solar cycle and seasonal variations of the Martian exospheric temperatures in the upper thermosphere and exosphere of Mars (at/above ~160 km). The dayside heat balance is primarily achieved by solar EUV-UV heating and molecular thermal conduction, with rather weak influence of CO_2 15 μm cooling [*Bougher et al*., 1990, 1999, 2009, S. W. Bougher et al., manuscript in final preparation, 2014]. Mechanical adiabatic heating and cooling due to upwelling (dayside) and downwelling (nightside) motion from the global thermospheric circulation (including impact of tides and gravity waves) play a relatively important role in the thermospheric structure [*Bougher et al*., 1990, 1999, 2000, 2009, S. W. Bougher et al., manuscript in final preparation, 2014].

The background thermosphere and ionosphere are supplied by the MTGCM for corresponding solar activity and orbital position case. According to this atmospheric input, the temperature of the Martian atmosphere increases slowly and becomes isothermal above ~160–200 km altitude (dependent on season), located near the bottom of the exosphere. The map of neutral temperature for the low solar activity and equinox case in Figure 3a shows the high temperatures along the terminators and near the polar regions and the low temperatures in low and middle latitudes on the nightside. The highest temperature located near the north pole on the morning terminator is about 270 K, and the lowest temperature is about 110 K located near the antisubsolar point and high latitudes on the southern hemisphere. The high-latitude region and most of the dayside region are found to display the global average exospheric temperature of about 170 K. The coriolis forces on the atmospheric circulation (as influenced by the planetary rotation) are evident; the zonal

©2014. American Geophysical Union. All Rights Reserved.

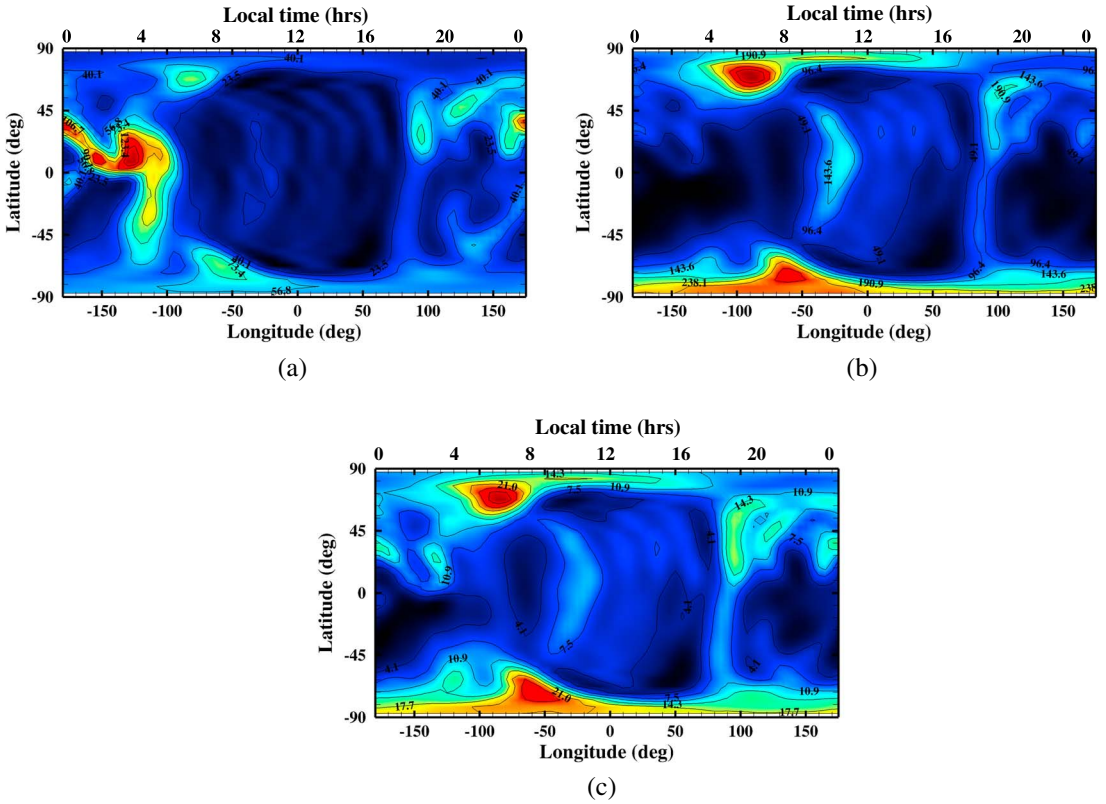

Figure 4. (a) Thermal O, (b) thermal CO_2, and (c) thermal CO density distributions for the low solar and equinox case near 200 km. The density is read as "(number on the contour) $\times 10^6$ cm^{-3}." The maximum densities are ~ 210×10^6 cm^{-3}, 880×10^6 cm^{-3}, and 47×10^6 cm^{-3} for O, CO^2, and CO, respectively, and are shown in dark red.

flow is minimum at the evening terminator and maximum at the morning terminator. Thermal lag, like that of Earth, appears as the offsets of peak temperatures from the subsolar point toward the midafternoon [e.g., *Bougher et al.*, 1999, 2000]. The "heat island" is also shown (about LT = 0200), which is due the convergence and adiabatic heating from subsiding flow by the modified thermospheric winds [*Bougher et al.*, 1990].

Our input background atmosphere for this work consists of three neutral species (O, CO_2, and CO) and three ionospheric species (e^-, O_2^+, and CO^+), and their densities are provided from 135 km to 200 km, as mentioned previously in the framework description section 2.3. Altitude profiles of the densities of thermosphere and ionosphere species are presented in Figures 3b and 3c, respectively, for several different solar zenith angles. The local variation of the background temperatures influences the distribution of the local background densities. As a result, the scale heights of the neutral and ion densities profiles become larger as solar zenith angle increases. This scale height variation is larger along a meridian than along the equator due to the larger temperature variation (about a factor of 1.5 between polar region and equator regions) for the equinox condition, the specific orbital position considered in this work.

4.2. Background Neutral Atmosphere/CO Density Distribution Comparison With O and CO_2

The major neutral constituents in the upper Martian thermosphere and exosphere are O atom and CO_2 molecule. CO_2 is the dominant neutral species in the lower thermosphere up to an altitude of about 180–220 km, depending on the solar activity. Because of the mass difference, O density (having a larger scale height) surpasses CO_2 density and becomes the dominant species in the upper thermosphere. As shown in Figure 4b, the maximum densities of CO_2 are situated in middle latitude in the north on the evening terminator and at high latitude near the pole regions. O density reaches its maximum on the nightside, from about midnight to LT = 0400 from low to middle latitude due to the strong convergence of the global wind system, whereas the minima are in the regions where the winds are weak or diverging (i.e., on the dayside

©2014. American Geophysical Union. All Rights Reserved.

from low to middle latitude, Figure 4a). While CO_2 density is well distributed spatially in accordance with the neutral temperature distribution (i.e., the maxima and minima are in the locations of high and low temperatures, respectively), O atoms are more efficiently transported by the atmospheric circulation due to their relatively lighter mass compared with CO_2. As shown in Figures 4a and 4b, the horizontal variation of O density is less than that of CO_2 density since O density tends to be more responsive to the global wind system than the background temperature.

Carbon monoxide is one of the major neutral molecules and an important source of hot carbon as it is photodissociated by solar EUV in the upper thermosphere. As shown in Figure 4c, the global distribution of CO exhibits features that reflect a mixture of the O and CO_2 distributions—more like CO_2 since CO is heavier than O but slightly lighter than CO_2. The maxima of CO density coincide with those of the CO_2 distribution (Figure 4b) plus some of the O maxima locations (Figure 4a) in middle latitude on the nightside. The minima are also in the low temperature and the diverging wind regions. The altitude profile of CO density (Figure 3b) shows the variation of the local density scale height at different solar zenith angles. The local scale height of CO density varies more along a meridian than along the equator. The local background temperature varies by about a factor of 1.5 from the subsolar point to the region near the north pole. The corresponding local scale height of CO density increases by a factor of ~1.3 as solar zenith angle increases. When the solar activity increases, the upper atmosphere absorbs more solar EUV fluxes and develops higher temperatures and stronger vertical winds, resulting in an expansion of thermosphere and enhancement of densities (i.e., increase of scale heights). More detailed study on this solar cycle and seasonal variability in the thermosphere and ionosphere is discussed in Paper II.

4.3. CO^+ Ionospheric Peak and Its Distribution Compared With O_2^+

The major species in the Martian ionosphere, O_2^+, is produced through photodissociation of major neutral species, CO_2, and charge exchange between CO_2^+ and O. *Valeille et al*. [2009a] showed that the horizontal distribution of O_2^+ density maxima is situated at the locations of CO_2 density maxima, where the peak density is found deep in the dayside thermosphere. Like O_2^+, CO^+ is a molecular ion, which follows a similar distribution pattern and variations with the solar cycle and seasons. The production of CO^+ is closely related to the densities of CO_2, the major background species below ~200 km altitude, and CO. The main source reactions in the Martian ionosphere are photoionization of CO and photodissociative ionization of CO_2,

$$CO + h\nu \rightarrow CO^+ + e,$$
$$CO_2 + h\nu \rightarrow CO^+ + O + e.$$

CO^+ is also produced by electron impact ionization of CO and electron impact dissociative ionization of CO_2. However, these last two reactions are not presently included in the MTGCM.

The major loss reaction of CO^+ ions is charge exchange between CO^+ and CO_2,

$$CO^+ + CO_2 \rightarrow CO_2^+ + CO,$$

which is a fast reaction. Charge exchange with O is another loss mechanism that removes CO^+ ions more effectively at higher altitude, where O is a major background species. As shown in the altitude profiles of the background densities from our input model (Figure 3c), the major production of CO^+ takes place where the parent molecules, CO and CO_2, are abundant. At lower altitude region, CO^+ ions are produced from the main source reactions and removed dominantly by charge exchange with CO_2. CO^+ density keeps increasing up to an altitude of ~180 km (for the equinox and solar minimum case), because the rate of the loss process by charge exchange between CO^+ and CO_2 decreases faster than the rate of the production by photoionization of CO, while the loss process by O is negligible. At higher altitudes, the production rate by CO photoionization decreases faster than the dominant loss process rate by O (charge exchange with O), resulting in the CO^+ density decrease with altitude. The peak height of CO^+ varies as solar zenith angle increases and solar activity and orbital position changes. As mentioned earlier, for the low solar activity and equinox case, the peak height is generally located above 200 km altitude because the effect of loss mechanisms on the net CO^+ density is minimized. Consequently, dissociative recombination of CO^+ is a nonnegligible source of nonthermal escape of hot carbon in the upper thermosphere and exosphere of Mars. On the dayside, the existence of the CO^+ ionospheric peak in the upper thermosphere implies that the overall global escape rate

©2014. American Geophysical Union. All Rights Reserved.

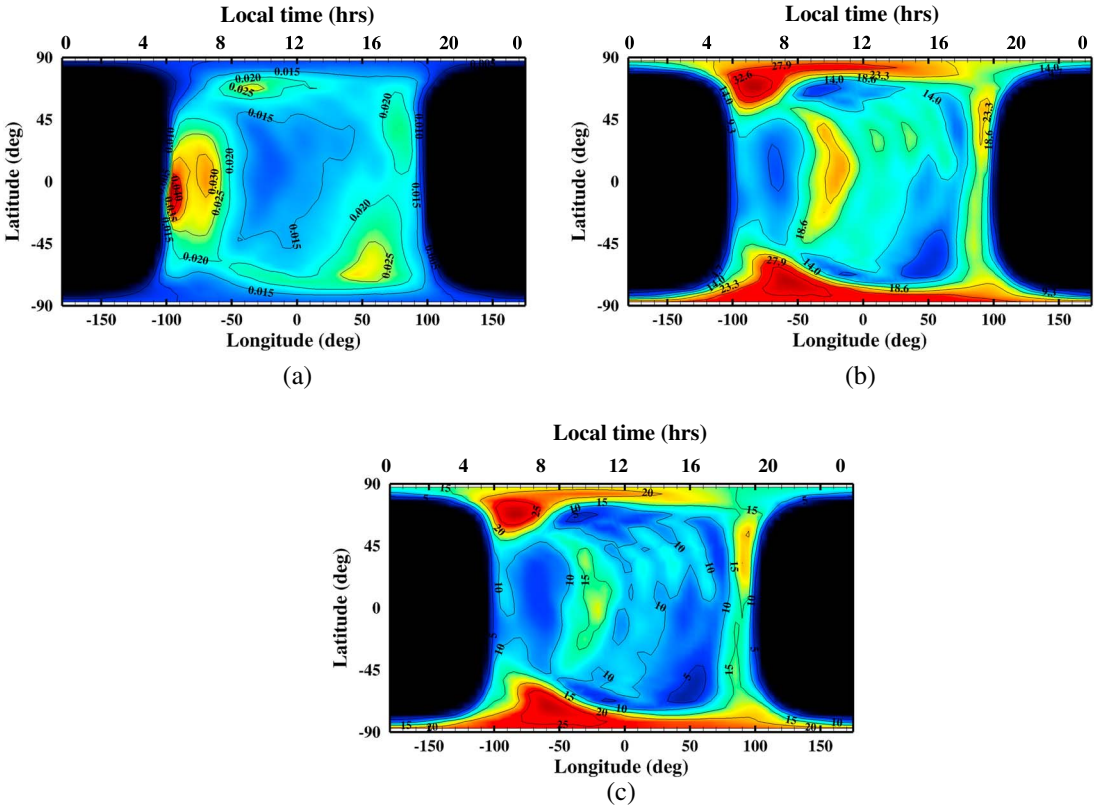

Figure 5. Density distributions near 200 km of (a) CO^+, (b) electron, and (c) O_2^+ for the low solar and equinox case. The contours show the density (cm^{-3}). The density is read as "(number on the contour) × 10^3 cm^{-3}." The maximum densities are ~ 41 × 10^3 cm^{-3}, 45 × 10^3 cm^{-3}, and 35 × 10^3 cm^{-3} for CO^+, electron, and O_2^+, respectively, and are shown in dark red.

of hot carbon resulting from dissociative recombination of CO^+ is quite sensitive to the background conditions (i.e., T_e, T_n, T_i, and $n(CO^+)$) near/above ~200 km.

Since all the atmospheric input (MTGCM) is extrapolated above 200 km according to the local density scale height, CO^+ density requires different extrapolation method to capture its density peak. Assuming that the density decreases exponentially with respect to the local density scale height above the peak altitude of CO^+, we estimated the density and density scale height at the peak altitude by adapting the features of the CO^+ density profiles (above 200 km) from other previous studies [*Fox*, 2004; *Fox and Bakalian*, 2001; *Fox and Hać*, 1999, 2009] for similar solar conditions. We modified our extrapolation scheme to include this estimated CO^+ density peak and make the CO^+ density decrease appropriately from the designated peak height with the approximate scale height. Since the CO^+ density remains full 3-D below 200 km, we expect that the results will not be significantly different from the possible results from a future atmospheric input model that can completely capture the CO^+ density peak.

The MTGCM assumes the photochemical equilibrium when solving the ionosphere of Mars. Above an altitude of 200 km, the densities of all the ions are extrapolated by the AMPS without considering the ion transport. The ion transport at higher altitude strongly influences O^+, the major ionospheric species above about 200 km. O_2^+ as well as CO^+ densities also diffuse by the ion transport at higher altitude. The extrapolated CO^+ density in our model already takes into account the ion transport indirectly since the referenced ion density profiles impose the upward velocity above an altitude where the ion transport is important.

Figures 5b and 5c show the horizontal distribution of electron and O_2^+ densities near 200 km. These spatial distribution patterns resemble those of neutral temperature on the dayside only, while CO^+ density pattern (Figure 5a) shows the inverse relation. As for the altitude profile, the horizontal distribution of CO^+ is also linked to that of the parent molecules, CO and CO_2. The local CO^+ ions are effectively removed by the fast

©2014. American Geophysical Union. All Rights Reserved.

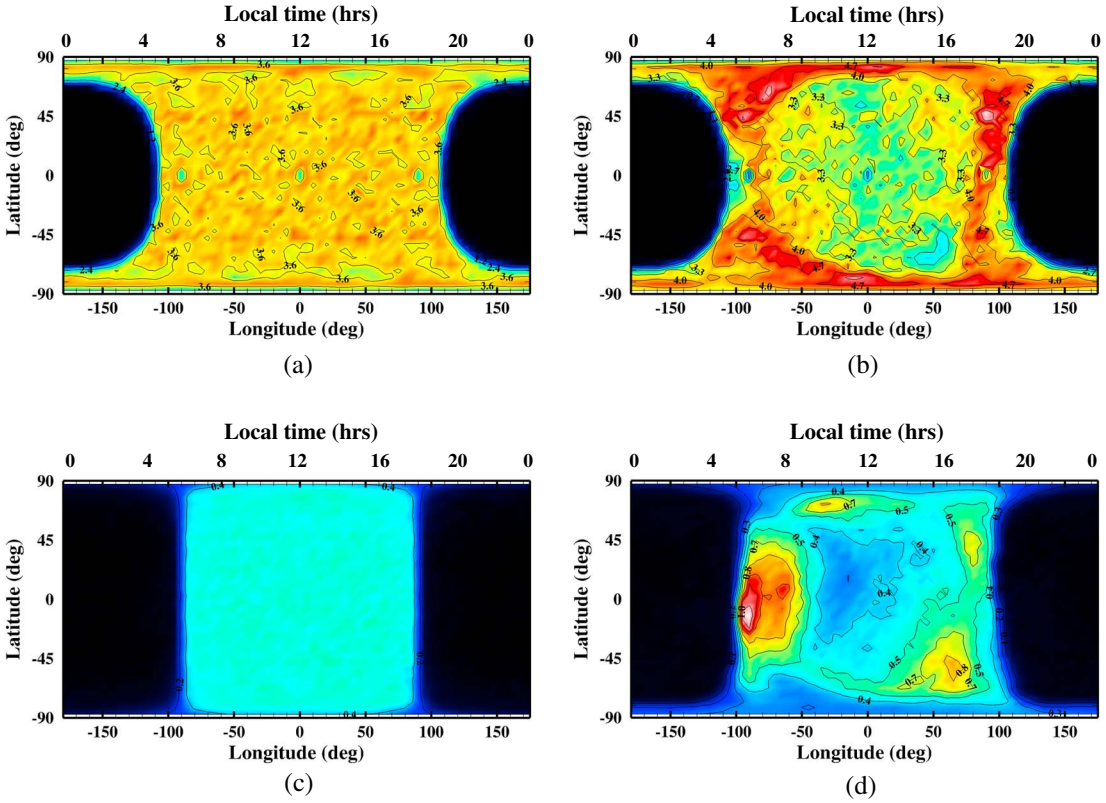

Figure 6. Latitude/longitude variations of simulated hot C density near 200 km in units of cubic centimeters produced from photodissociation of CO using (a) 1-D and (b) 3-D atmospheric inputs and from dissociative recombination of CO^+ using (c) 1-D and (d) 3-D atmosphere inputs.

charge exchange with CO_2 and O. As a result, the spatial distribution of CO^+ displays anticorrelation with O and CO_2 distribution patterns.

The production rate of hot carbon from dissociative recombination of CO^+ is controlled by three factors: CO^+ and electron densities and the dissociative recombination coefficient, which varies as $T_e^{-0.55}$. Indeed, hot carbon density peaks where the CO^+ density maxima and electron temperature minima are located. The maximum and minimum electron densities are situated approximately at high and low neutral temperature regions. This is an additional implication of the analysis of the MGS occultations by *Bougher et al*. [2001, 2004], which showed that electron density peak heights could be a proxy for the longitudinal variations of the underlying neutral atmospheric structure over the seasons.

5. Results and Discussion

We have simulated the global distribution of hot carbon resulting from the two main source reactions, photodissociation of CO and dissociative recombination of CO^+. The coupled 3-D AMPS and the 3-D MTGCM provide a detailed description of the variations of the macroscopic parameters from a local to global perspective, which is essential for understanding the Martian hot exosphere more precisely and practically. As for the purpose of this work, the following discussion will investigate the different responses from the different source reactions and the spatial variation of the hot carbon corona for the specific solar condition and Mars season, low solar activity, and equinox ($F10.7 = 70$; $L_s = 180°$).

5.1. Effects of the 3-D Thermosphere/Ionosphere

The hot carbon exosphere at Venus was observed by the UV spectrometer aboard the Pioneer Venus Orbiter [e.g., *Paxton*, 1985; *Stewart*, 1980]. The Martian hot carbon corona has not been observed yet but modeled by several modelers [e.g., *Fox and Hać*, 1999; *Nagy et al*., 2001] using different numerical approaches. These modeling efforts have estimated and simulated the global loss of carbon. However, the previous models have

©2014. American Geophysical Union. All Rights Reserved.

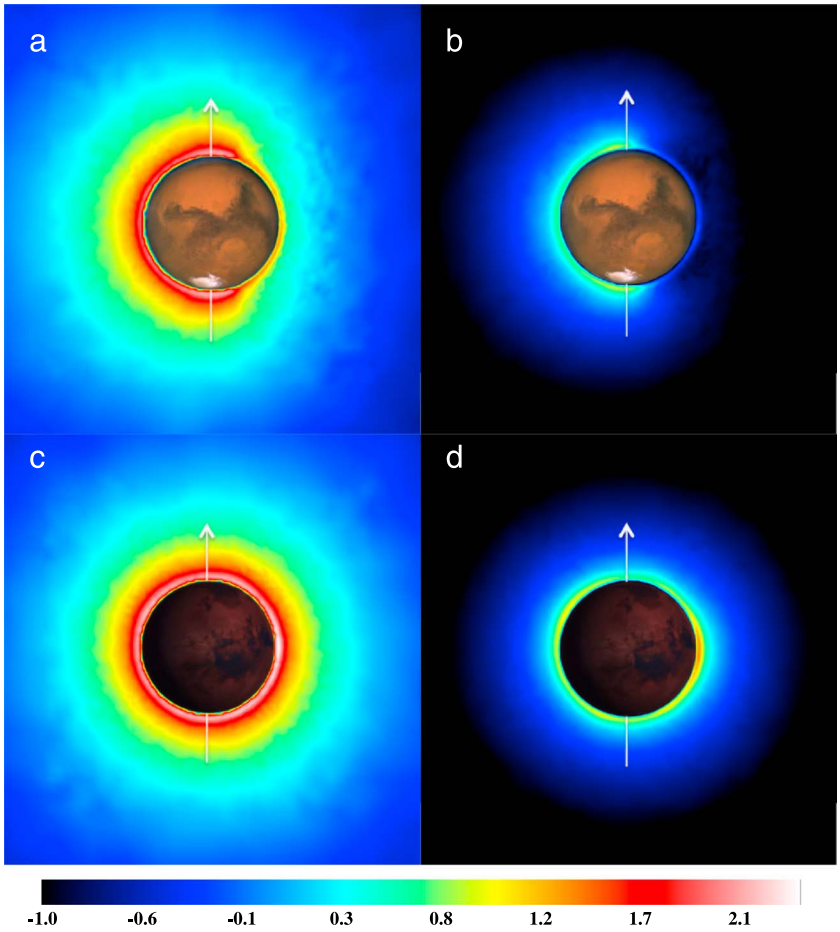

Figure 7. Sun-Mars meridian plane view of hot C density with the Sun on the left from (a) photodissociation of CO and (b) dissociative recombination of CO^+ and tail-to-Sun view of hot C density from (c) photodissociation of CO and (d) dissociative recombination of CO^+ for the solar low and equinox case. The contours show the hot C density (cm^{-3}) in log scale.

lacked the important influences of the thermospheric and ionospheric structures and their variability, which can only be described by the 3-D features of the atmosphere. These 3-D features include the planetary rotation, global scale dynamics, sharp gradients near the terminators, hemispheric asymmetries, and polar warming effects. Mars rotates at a speed that is comparable to the average thermospheric wind speed (zonal and meridional winds), which is about 240 m/s. This speed is fast enough to enable the rotation to be as effective (to the same degree) as the thermospheric winds for impacting the hot particle motion in the upper atmosphere, the structure of hot density profiles, and, in turn, the return flux of hot particles back to the thermosphere [*Valeille et al*., 2009a]. As mentioned in the earlier sections, the full 3-D description of hot corona using 3-D thermosphere/ionosphere inputs allows one to capture more realistic features resulting from the main source mechanisms and interactions between hot species and the Martian upper atmosphere.

In addition to the effect of the planetary rotation and thermospheric winds, the spatial variation of hot carbon production is determined by the local thermospheric and ionospheric features. The production rate of hot carbon from photodissociation of CO follows the horizontal distribution of CO density. As mentioned, due to its slightly lighter mass (than that of CO_2), the distribution of thermal CO molecule exhibits the characteristics of both CO_2 and O, which are more responsive to the background temperature and the atmospheric circulation, respectively (section 4.2, Figure 4). In the same sense, different ionospheric asymmetries for the different ion species uniquely affect the spatial variations of the dissociative recombination of CO^+ production rate (section 4.3, Figure 5).

©2014. American Geophysical Union. All Rights Reserved.

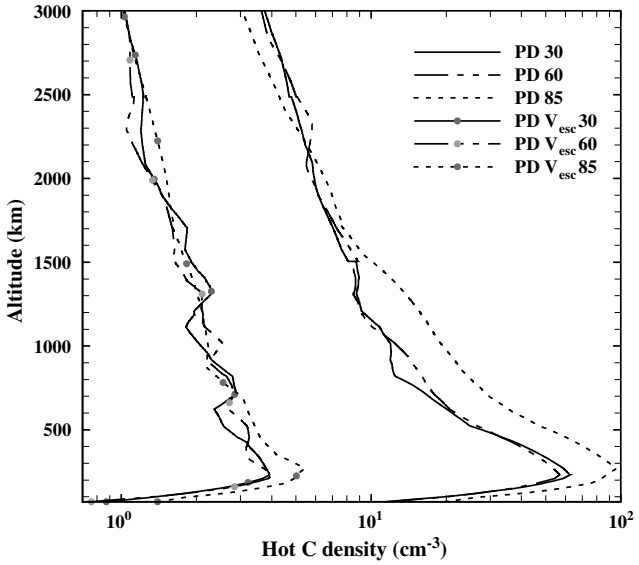

Figure 8. Density profiles of hot C (solid) and the fraction of hot C that have their velocity larger than the local escape speed (filled circle, V_{esc}) resulting from (a) photodissociation of CO and (b) and dissociative recombination of CO^+ for different SZA (30° (solid), 60° (dash-dotted), and 85° (dotted)) for the solar low and equinox case. Hot C profiles are extracted north poleward (along the noon meridian) for the photodissociation of CO case and along the equatorial west for the dissociative recombination of CO^+ case.

Figure 6 shows the hot carbon density distributions by two source reactions (photodissociation of CO and dissociative recombination of CO^+) simulated with the atmosphere that is spherically symmetric over the dayside (1-D, Figures 6a and 6c) and full 3-D atmospheric inputs (Figures 6b and 6d). For the purpose of comparison between the effects of 1-D and 3-D atmospheric input, we extracted a column of atmosphere from our 3-D atmospheric input at solar zenith angle (SZA) 60° and distributed over the entire dayside. We chose this particular column of the atmosphere by assuming that the atmosphere at SZA 60° is the representative of the average over the dayside. Except for the small fluctuation of the density caused by the statistical noise in the 1-D computation, the full 3-D atmosphere input case evidently displays many important local features that the dayside-averaged case does not display.

As expected, the hot carbon density produced by photodissociation of CO (Figure 6b) is spatially distributed in a pattern that is similar to the thermal CO distribution. The hot carbon atom production is continued onto the nightside (over the polar regions) except in the regions of the planet's shadow. Most of the escape happens on the dayside and is enhanced along the evening terminator, near the polar regions, and in middle and high latitudes on the morning terminator due to the subsiding atmospheric flow that impacts CO density.

The hot carbon resulting from dissociative recombination of CO^+ (Figure 6d) is characterized by its local maximum escape located near the equator on the morning terminator, where the maxima of CO^+ density and the minima of electron temperature are located. The overall spatial distribution is very different from that of the hot oxygen, which is produced by dissociative recombination of O_2^+ (the major ion).

5.2. Hot Carbon Density

Hot carbon atoms are produced through various possible source mechanisms. As discussed in section 3, the majority of hot carbon is produced by photodissociation of CO, and the next nonnegligible source is assumed to be dissociative recombination of CO^+ in this study. The different source reactions contribute different

©2014. American Geophysical Union. All Rights Reserved.

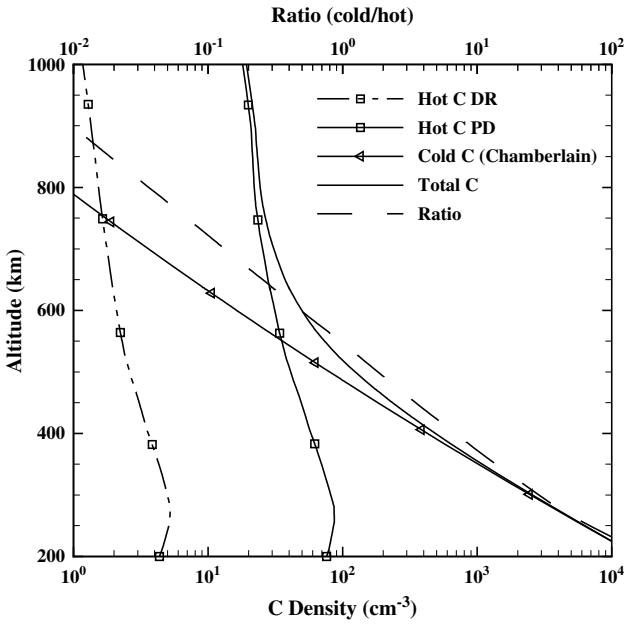

Figure 9. Total C (solid) density profile for the solar low and equinox case. Density profiles of the hot C produced from photodissociation of CO (solid, square) and dissociative recombination of CO^+ (dash-dotted, square) are extracted at SZA 60°. Thermal C (cold C) density profile (solid, triangle) is estimated by using the Chamberlain model. The cold C/hot C ratio is shown in black dashed line.

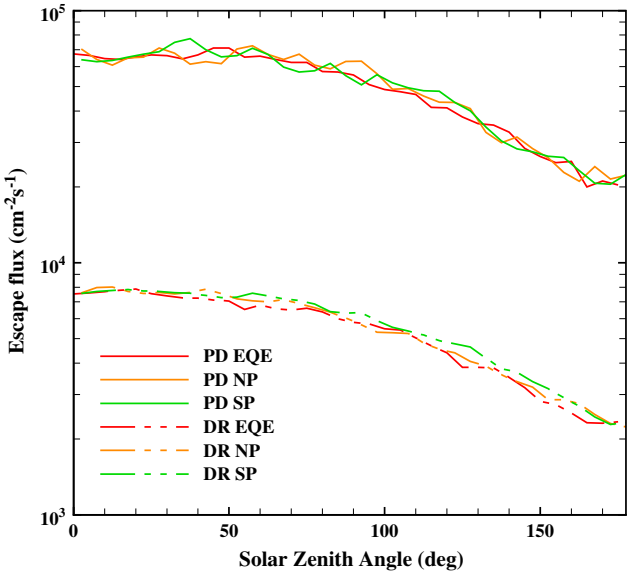

Figure 10. Escape fluxes of hot C produced by two sources, photodissociation of CO (solid) and dissociative recombination of CO^+ (dash-dotted), are calculated at different locations around the planet as a function of SZA at an altitude of 3 Mars radii. Computations have been done over the equatorial east (EQE, red), the north pole (NP, orange), and the south pole (SP, green).

features to the Martian hot carbon corona along with the inherent planetary physics (e.g., planetary rotation and orbital position).

One example of the characteristic features on the shape of hot corona related to the source reactions is shown in Figures 7c and 7d. Unlike the near-symmetrical shape of hot corona (in tail-to-Sun view) in photodissociation of CO case, dissociative recombination of CO^+ case displays a pronounced density enhancement on the morning terminator.

Figure 7 presents the hot carbon corona computed separately by each source reaction. It is logical to expect the overall shape of hot corona in the meridional plane to exhibit the nonaxisymmetric oblong shape. Since both source reactions are photochemical mechanisms, the density distributions from both reactions enhance globally over the dayside, decreasing exponentially with increasing distance from the planet. The sharp density gradients over the polar regions are shown where the hot density increases slightly near the terminators and decreases abruptly on the nightside. The production of hot carbon does not take place on the nightside, but the nightside hot population exists in the simulated results due to the hot carbon produced on the dayside, impacting the nightside and scattering back upward or "bouncing" as described by *Valeille et al.* [2009a]. The maximum hot carbon density produced by photodissociation of CO (Figure 7a) on the dayside is $\sim 3 \times 10^2$ cm^{-3} near the terminators. The density decreases by about an order of magnitude on the nightside. The dissociative recombination of CO^+ case also has similar diurnal variation but with the density maximum of $\sim 1 \times 10^1$ cm^{-3} (Figure 7b).

The structure of the hot carbon density profile at lower altitudes is affected mostly by the thermospheric winds and planetary rotation. Figures 8a and 8b show the density profiles of the hot carbon produced from photodissociation of CO and dissociative recombination of

©2014. American Geophysical Union. All Rights Reserved.

Table 1. Escape Fluxes of Hot Carbon From Two Sources at Different Solar Zenith Angles at an Altitude of 3 Mars Radii

	Solar Zenith Angle				
Escape Flux (10^4 cm^{-2} s^{-1})[a]	30°	60°	90°	120°	150°
Photodissociation of CO	6.63	6.60	5.56	4.11	2.64
Dissociative recombination of CO^+	0.74	0.68	0.58	0.40	0.28

[a]Fluxes are in 10^4 cm^{-2} s^{-1}, computed over the equatorial east direction.

CO^+, respectively, for the different solar zenith angles. In each plot, the hot carbon density is calculated with two different setting for $V_{threshold}$, twice the local thermal speed as usual and the local escape speed specifically to obtain the fraction of the total hot carbon population. The hot density from both source reactions peaks above ~270 km altitude for the low solar activity and equinox case. The peak altitude of the hot carbon density increases from about 250 km to 300 km as the solar zenith angle increases since the altitude of the source peaks (thermal CO and CO^+) increases with solar zenith angle. The nascent hot carbon that exceeds the local escape speed is ~10% of the local hot carbon population near the peak altitude of hot carbon density for both source reactions.

Thermal atomic carbon is one of the minor neutral atoms in the Martian atmosphere. According to Figure 5 in the study by *Fox* [2004] (density profiles of the minor neutral species for the low solar activity model), the peak altitude of the thermal carbon density is at ~140 km altitude, and the density decreases to about 2×10^2 cm^{-3} at 400 km. Compared to our modeled hot carbon density, which peaks at around 250–300 km, the thermal C dominates the carbon population over hot C by more than about 2 orders of magnitude near 200 km. Since our thermosphere/ionosphere input model does not simulate thermal C, we have estimated the thermal (cold) C profile by using the Chamberlain model [*Chamberlain*, 1963] (Figure 9). As a parallel study of the total O density profile by *Valeille et al.* [2010a], Figure 9 shows the altitude profiles of hot and cold C for the approximated transition region, where the C population makes transition from the cold- to the hot-dominated regimes. This transition region is considered to be between 230 km and 900 km for the C population for the case considered in this work. The altitude of this region is expected to vary with solar activity or orbital position. We estimate that the ratio of hot C to cold C densities becomes over 1 above the altitude of about 550 km. Therefore, the total carbon population below about 500 km altitude is considered to be dominated by thermal C.

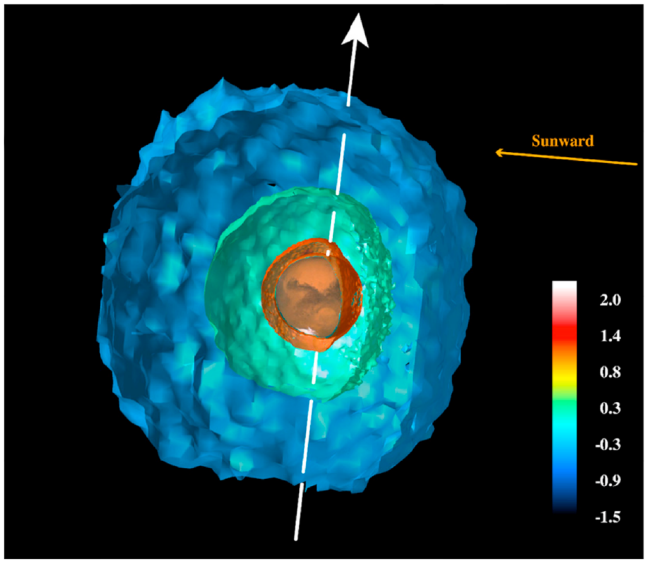

Figure 11. Three-dimensional view of hot carbon corona with the Sun in the direction where the orange arrow points. White arrow points to the north pole of the planet. Three isosurfaces represent the log density of hot carbon density surfaces both from photodissociation of CO and dissociative recombination of CO^+. Isosurfaces are at $\log_{10}$ (cm^{-3}) = −0.5 (~0.3 cm^{-3}), 0.2 (~1.6 cm^{-3}), and 1.2 (~15.8 cm^{-3}).

Figure 10 presents the escape flux computed for each source reaction at 3 Mars radii as a function of solar zenith angle. Although hot carbon production does not take place on the nightside, the effect of gravity and the ubiquitously cumulative collisional interaction in the transitional region result in the escape flux over the nightside (bouncing effect).

Three different extreme locations are chosen to compute the escape fluxes: equatorial eastward, north poleward (along the noon meridian), and south poleward (along the noon meridian). Since the local parameters are averaged over a larger area as the distance from the planet increases, the interhemispheric variation is negligible in our computation. The tabulated escape fluxes (Table 1) respect to SZA of 30° increments show that the diurnal difference is about a factor of 3.2 for both source reaction cases. The effect of

©2014. American Geophysical Union. All Rights Reserved.

photodissociation mechanisms on the escape flux is about an order of magnitude larger than that of dissociative recombination.

The hot carbon corona is visualized in 3-D in Figure 11. The isosurfaces at different altitudes exhibit the near-spherical shape of the distribution over the dayside and abrupt decrease over the terminators and nightside. The shape of isosurface shows the lesser degree of the oblong appearance with the increasing distance from the planet.

6. Conclusions

We have coupled our 3-D DSMC kinetic model, AMPS, with the 3-D MTGCM thermosphere/ionosphere model to simulate the Martian hot carbon corona. This combination of two models provides a self-consistent global description of the Martian upper thermosphere and exosphere. For the purpose of the study, a simulation for the fixed condition, low solar activity, and equinox, is considered. Among the various sources of hot carbon atoms, we have considered the two important mechanisms: photodissociation of CO and dissociative recombination CO^+.

The effects of the background temperatures and global atmospheric circulation are presented in the resulting distributions of energetic carbon atom. The spatial distribution of the neutral atmospheric constituent density is more responsive to the background temperatures or winds, depending on the mass of the species. The resulting hot carbon density is distributed with respect to the local production rate, which can be characterized by the combination of local macroscopic parameters from the MTGCM.

We have compared the hot carbon corona produced using 1-D and full 3-D atmospheric inputs. The main advantage of using full 3-D thermosphere/ionosphere input is the ability of incorporating the effects of nonaxisymmetric features (e.g., planetary rotation and thermospheric winds), which are inherently absent in other 1-D atmospheric models. These 3-D features are found to greatly impact the structure of the hot carbon density profiles and shape of the hot carbon corona.

Our simulation estimated the global escape rates of hot C for the low solar activity and equinox condition for the two source reactions and found them to be 4.94×10^{23} s^{-1} (~84%) and 0.96×10^{23} s^{-1} (~16%) for the photodissociation and dissociative recombination cases, respectively.

In the work of Paper II, the Martian hot carbon corona is investigated in great detail with respect to solar cycle and seasonal variation, which is substantial for understanding the dynamically changing Martian atmosphere. Paper II also discusses and compares the results from the previous models with our model results.

Finally, we expect greatly renewed interest in studying the physics of Martian hot coronae (both O and C) in depth with the in situ and remote measurements of the upper atmosphere from the Mars Atmosphere and Volatile Evolution mission.

Acknowledgments
This work has been supported by NASA Mars Fundamental Research Program grant NNX09AL26G. Resources for all simulations in this work have been provided by NASA High-End Computing Capability (HECC) project at NASA Advanced Supercomputing (NAS) Division.

References

Acuna, M. H., et al. (1998), Magnetic field and plasma observations at Mars: Initial results of the Mars Global Surveyor mission, *Science*, *279*, 1676, doi:10.1126/science.279.5357.1676.

Bakalian, F. (2006), Production of hot nitrogen atoms in the Martian thermosphere, *Icarus*, *183*, 69–78, doi:10.1016/j.icarus.2006.02.005.

Bell, J. M., S. W. Bougher, and J. R. Murphy (2007), Vertical dust mixing and the interannual variations in the Mars thermosphere, *J. Geophys. Res.*, *112*, E12002, doi:10.1029/2006JE002856.

Berger, M. J., and P. Colella (1989), Local adaptive mesh refinement for shock hydrodynamics, *J. Comput. Phys.*, *82*, 64–84.

Bird, G. A. (1994), *Molecular Gas Dynamics and the Direct Simulation of Gas Flows*, Clarendon Press, Oxford.

Bougher, S. W., R. G. Roble, E. C. Ridley, and R. E. Dickinson (1990), The Mars thermosphere 2. General circulation with coupled dynamics and composition, *J. Geophys. Res.*, *95*, 14,811–14,827, doi:10.1029/JB095iB09p14811.

Bougher, S. W., S. Engel, R. G. Roble, and B. Foster (1999), Comparative terrestrial planet thermospheres 2. Solar cycle variation of global structure and winds at equinox, *J. Geophys. Res.*, *104*, 16,591–16,611, doi:10.1029/1998JE001019.

Bougher, S. W., S. Engel, R. G. Roble, and B. Foster (2000), Comparative terrestrial planet thermospheres. 3. Solar cycle variation of global structure and winds at solstices, *J. Geophys. Res.*, *105*, 17,669–17,692, doi:10.1029/1999JE001232.

Bougher, S. W., S. Engle, D. P. Hinson, and J. M. Forbes (2001), Mars Global Surveyor radio science electron density profiles: Neutral atmosphere implications, *Geophys. Res. Lett.*, *28*, 3091–3094, doi:10.1029/2001GL012884.

Bougher, S. W., R. G. Roble, and T. J. Fuller-Rowell (2002), Simulations of the upper atmospheres of the terrestrial planets, in *Atmospheres in the Solar System: Comparative Aeronomy*, edited by M. Mendillo, A. F. Nagy, and J. H. Waite, pp. 261–288, AGU, Washington, D. C.

Bougher, S. W., S. Engel, D. P. Hinson, and J. R. Murphy (2004), MGS Radio Science electron density profiles: Interannual variability and implications for the neutral atmosphere, *J. Geophys. Res.*, *109*, E03010, doi:10.1029/2003JE002154.

Bougher, S. W., J. M. Bell, J. R. Murphy, M. A. López-Valverde, and P. G. Withers (2006), Polar warming in the Mars thermosphere: Seasonal variations owing to changing insolation and dust distributions, *Geophys. Res. Lett.*, *32*, L02203, doi:10.1029/2005GL024059.

©2014. American Geophysical Union. All Rights Reserved.

Bougher, S. W., P.-L. Blelly, M. Combi, J. L. Fox, I. Mueller-Wodarg, A. Ridley, and R. G. Roble (2008), Neutral upper atmosphere and ionosphere modeling, *Space Sci. Rev.*, *139*, 107–141, doi:10.1007/s11214-008-9401-9.
Bougher, S. W., T. M. McDunn, K. A. Zoldak, and J. M. Forbes (2009), Solar cycle variability of Mars dayside exospheric temperatures: Model evaluation of underlying thermal balances, *Geophys. Res. Lett.*, *36*, L05201, doi:10.1029/2008GL036376.
Carr, M. H. (1986), Mars: A water-rich planet?, *Icarus*, *68*, 187–216.
Chamberlain, J. W. (1963), Planetary coronae and atmospheric evaporation, *Planet. Space Sci.*, *11*, 901–960.
Chassefiére, E., F. Leblanc, and B. Langlais (2007), The combined effects of escape and magnetic field histories at Mars, *Planet. Space Sci.*, *55*, 343–257, doi:10.1016/j.pss.2006.02.003.
Cipriani, F., F. Leblanc, and J. J. Berthelier (2007), Martian corona: Nonthermal sources of hot heavy species, *J. Geophys. Res.*, *112*, E07001, doi:10.1029/2006JE002818.
Combi, M. R. (1996), Time-dependent gas kinetics in tenuous planetary atmosphere: The cometary coma, *Icarus*, *123*, 297–226.
Crifo, J.-F., G. A. Loukianov, A. V. Rodionov, and V. V. Zakharov (2005), Direct Monte Carlo and multifluid modeling of the circumnuclear dust coma: Spherical grain dynamics revisited, *Icarus*, *176*, 192–219, doi:10.1016/j.icrus.2005.01.003.
Feldman, P. D., et al. (2011), Rosetta-Alice observations of exospheric hydrogen and oxygen on Mars, *Icarus*, *214*, 394–399, doi:10.1016/j.icarus.2011.06.013.
Forbes, J. M., A. F. C. Bridger, S. W. Bougher, M. E. Hagan, J. L. Hollingsworth, G. M. Keating, and J. Murphy (2002), Nonmigrating tides in the thermosphere of Mars, *J. Geophys. Res.*, *107*(E11), 5113, doi:10.1029/2001JE001582.
Forget, F., F. Montmessin, J.-L. Bertaux, F. González-Galindo, S. Lebonnois, E. Quémerais, A. Reberac, E. Dimarells, and M. A. López-Valverde (2009), Density and temperatures of the upper Martian atmosphere measured by stellar occultations with Mars Express SPICAM, *J. Geophys. Res.*, *114*, E01004, doi:10.1029/2008JE003086.
Fox, J. L. (1993), The production and escape of nitrogen atoms on Mars, *J. Geophys. Res.*, *98*, 3297–3310, doi:10.1029/92JE02289.
Fox, J. L. (1997), Spectrum of hot O at the exobases of the terrestrial planets, *J. Geophys. Res.*, *102*, 24,005–24,011, doi:10.1029/97JA02089.
Fox, J. L. (2004), CO_2^+ dissociative recombination: A source of thermal and nonthermal C on Mars, *J. Geophys. Res.*, *109*, A08306, doi:10.1029/2004JA010514.
Fox, J. L., and F. M. Bakalian (2001), Photochemical escape of atomic carbon from Mars, *J. Geophys. Res.*, *106*, 28,785–28,795, doi:10.1029/2001JA000108.
Fox, J. L., and J. H. Black (1989), Photodissociation of CO in the thermosphere of Venus, *Geophys. Res. Lett.*, *16*, 291–294, doi:10.1029/GL016i004p00291.
Fox, J. L., and A. B. Hać (1997), The N-15/N-14 isotope fractionation in dissociative recombination of N-2(+), *J. Geophys. Res.*, *104*, 24,729–24,738, doi:10.1029/1999JA900330.
Fox, J. L., and A. B. Hać (1999), Velocity distributions of C atoms in CO^+ dissociative recombination: Implications for photochemical escape of C from Mars, *J. Geophys. Res.*, *104*, 24,729–24,737, doi:10.1029/1999JA900330.
Fox, J. L., and A. B. Hać (2009), Photochemical escape of oxygen from Mars: A comparison of the exobase approximation to a Monte Carlo method, *Icarus*, *204*, 527–544, doi:10.1016/j.icarus.2009.07.005.
Haberle, R. M., M. M. Joshi, J. R. Murphy, J. R. Barnes, J. T. Schofield, G. Wilson, M. Lopez-Valverde, J. L. Hollingsworth, A. F. C. Bridger, and J. Schaeffer (1999), General circulation model simulations of the Mars Pathfinder atmospheric structure investigation/meteorology data, *J. Geophys. Res.*, *104*, 8957–8974, doi:10.1029/1998JE900040.
Hanson, W. B., S. Sanatani, and D. R. Zuccaro (1977), The Martian ionosphere as observed by the Viking Retarding Potential Analyzers, *J. Geophys. Res.*, *82*, 4351–4363, doi:10.1029/JS082i028p04351.
Hochstim, A. R. (1969), *Kinetic Processes in Gases and Plasmas*, Academic Press, New York.
Hodges, R. R. (2000), Distributions of hot oxygen for Venus and Mars, *J. Geophys. Res.*, *105*, 6971–6981, doi:10.1029/1999JE001138.
Hodges, R. R. (2002), The rate of loss of water from Mars, *Geophys. Res. Lett.*, *29*(3), 1038, doi:10.1029/2001GL013853.
Huebner, W. F., J. J. Keady, and S. P. Lyon (1992), Solar photo rates for planetary atmospheres and atmospheric pollutants, *Astrophys. Space. Sci.*, *195*, 1–294.
Jakosky, B. M. (1991), Mars volatile evolution: Evidence from stable isotopes, *Icarus*, *96*, 14–31.
Jakosky, B. M., and J. H. Jones (1997), The history of Martian volatiles, *Rev. Geophys.*, *35*, 1–16, doi:10.1029/96RG02903.
Keating, G. M., et al. (2003), Brief review on the results obtained with the MGS and Mars Odyssey 2001 Accelerometer Experiments, paper presented at International Workshop: Mars Atmosphere Modeling and Observations, Inst. de Astrofis. De Andalucia, Granada, Spain, 13–15 Jan.
Kim, J., A. F. Nagy, J. L. Fox, and T. E. Cravens (1998), Solar cycle variability of hot oxygen atoms at Mars, *J. Geophys. Res.*, *103*, 29,339–29,342, doi:10.1029/98JA02727.
Krupenie, P. H., and S. Weissman (1965), Potential-energy curves for CO and CO^+, *J. Chem. Phys.*, *43*, 1529, doi:10.1063/1.1696966.
Leblanc, F., and R. E. Johnson (2002), Role of molecular species in pickup ion sputtering of the Martian atmosphere, *J. Geophys. Res.*, *107*(E2), 5010, doi:10.1029/2000JE001473.
Lee, Y., M. R. Combi, V. Tenishev, and S. W. Bougher (2012), Global dynamics of hot atomic oxygen in Mars' upper atmosphere and comparison with recent observation, Abstract #SA51A-2146 presented at 2012 Fall Meeting, AGU, San Francisco, Calif., 3–7 Dec.
López-Valverde, M. A., D. T. Edwards, M. López-Puertas, and C. Roldán (1998), Non-local thermodynamic equilibrium in general circulation models of the Martian atmosphere 1. Effects of the local thermodynamic equilibrium approximation on thermal cooling and solar heating, *J. Geophys. Res.*, *103*, 16,799–16,811, doi:10.1029/98JE01601.
Luhmann, J. G. (1992), Mars atmosphere evolution: Escape to space, in *Workshop on the Martian Surface and Atmosphere Through Time*, pp. 91–92, Lunar and Planetary Inst., Houston, Tex.
Markelov, G. N., Y. V. Skorov, and H. U. Keller (2006), DSMC modeling of dusty innermost cometary atmosphere around non-spherical nucleus, *AIAA*, doi:10.2514/6.2006-3392.
McDunn, T. L., S. W. Bougher, J. Murphy, M. D. Smith, F. Forget, J.-L. Bertaux, and F. Montmessin (2010), Simulating the density and thermal structure of the middle atmosphere (~80-130 km) of Mars using the MGCM-MTGCM: A comparison with MEX/SPICAM observations, *Icarus*, *206*, 5–17, doi:10.1016/j.icarus.2009.06.034.
McElroy, M. B. (1972), Mars: An evolving atmosphere, *Science*, *175*, 443–445.
Melosh, H. J., and A. M. Vickery (1989), Impact erosion of the primordial atmosphere of Mars, *Nature*, *338*, 487–489.
Morgan, D. D., D. A. Gurnett, D. L. Kirchner, J. L. Fox, E. Nielsen, and J. J. Plaut (2008), Variation of the Martian ionospheric electron density from Mars Express radar soundings, *J. Geophys. Res.*, *113*, A09303, doi:10.1029/2008JA013313.
Nagy, A. F., M. W. Liemohn, J. L. Fox, and J. Kim (2001), Hot carbon densities in the exosphere of Mars, *J. Geophys. Res.*, *106*, 21,565–21,568, doi:10.1029/2001JA000007.

©2014. American Geophysical Union. All Rights Reserved.

Nier, A. O., and M. B. McElroy (1977), Composition and structure of Mars' upper atmosphere: Results from the neutral mass spectrometers on Viking 1 and 2, *J. Geophys. Res.*, *82*, 28.

Paxton, L. J. (1985), Pioneer Venus Orbiter ultraviolet spectrometer limb observations: Analysis and interpretation of the 166- and 156-nm data, *J. Geophys. Res.*, *90*, 5089–5096, doi:10.1029/JA090iA06p05089.

Pepin, R. O. (1994), Evolution of the Martian atmosphere, *Icarus*, *111*, 289–304.

Rosén, S., et al. (1998), Absolute cross sections and final-state distributions for dissociative recombination and excitation of CO + (v = 0) using an ion storage ring, *Phys. Rev. A*, *57*, 4462.

Smith, E. J., L. Davis Jr., P. J. Coleman Jr., and D. E. Jones (1965), Magnetic field measurements near Mars, *Science*, *149*(3689), 1241–1242.

Stewart, A. I. F. (1980), Design and operation of the Pioneer Venus Orbiter ultraviolet spectrometer, *IEEE Trans. Geosci. Remote Sens.*, *GE-18*, 65–70, doi:10.1109/TGRS.1980.350283.

Tenishev, V., M. R. Combi, and B. Davidsson (2008), A global kinetic model for cometary comae. The evolution of the coma of the Rosetta target comet Churyumov–Gerasimenko throughout the mission, *Astrophys. J.*, *685*, 659–677.

Tenishev, V., M. R. Combi, and M. Rubin (2011), Numerical simulation of dust in a cometary coma: Application to comet 67P/Churyumov-Gerasimenko, *Astrophys. J.*, *732*, 104, doi:10.1088/0004-637X/732/2/104.

Tenishev, V., M. Rubin, O. J. Tucker, M. R. Combi, and M. Sarantos (2013), Kinetic modeling of sodium in the lunar exosphere, *Icarus*, *226*, 1538–1549, doi:10.1016/j.icarus.2013.08.021.

Torr, M. R., D. G. Torr, and R. A. Omg (1979), Ionization frequencies for major thermospheric constituents as a function of solar cycle 21, *Geophys. Res. Lett.*, *6*, 10.

Valeille, A., V. Tenishev, S. W. Bougher, M. R. Combi, and A. F. Nagy (2009a), Three-dimensional study of Mars upper thermosphere/ionosphere and hot oxygen corona: 1. General description and results at equinox for solar low conditions, *J. Geophys. Res.*, *114*, E11005, doi:10.1029/2009JE003388.

Valeille, A., M. R. Combi, S. W. Bougher, V. Tenishev, and A. F. Nagy (2009b), Three-dimensional study of Mars upper thermosphere/ionosphere and hot oxygen corona: 2. Solar cycle, seasonal variations, and evolution over history, *J. Geophys. Res.*, *114*, E11006, doi:10.1029/2009JE003389.

Valeille, A., M. R. Combi, V. Tenishev, S. W. Bougher, and A. F. Nagy (2010a), A study of suprathermal oxygen atoms in Mars upper thermosphere and exosphere over the range of limiting conditions, *Icarus*, *206*, 18–27, doi:10.1016/j.icarus.2008.08.018.

Valeille, A., M. R. Combi, V. Tenishev, S. W. Bougher, and A. F. Nagy (2010b), Water loss and evolution of the upper atmosphere and exosphere over Martian history, *Icarus*, *206*, 28–39, doi:10.1016/j.icarus.2009.04.036.

Wilson, R. J. (2002), Evidence for nonmigrating thermal tides in the Mars upper atmosphere from the Mars Global Surveyor Accelerometer Experiment, *Geophys. Res. Lett.*, *29*(7), 1120, doi:10.1029/2001GL013975.

Withers, P., and M. Mendillo (2005), Response of peak electron densities in the Martian ionosphere to day-to-day changes in solar flux due to solar rotation, *Planet. Space Sci.*, *53*, 1402–1418, doi:10.1016/j.pss.2005.07.010.

Withers, P., S. W. Bougher, and G. M. Keating (2003), The effects of topographically-controlled thermal tides in the Martian upper atmosphere as seen by the MGS accelerometer, *Icarus*, *164*, 14–32, doi:10.1016/S0019-1035(03)00135-0.

Withers, P., M. Mendillo, D. P. Hinson, and K. Cahoy (2008), Physical characteristics and occurrence rates of meteoric plasma layers detected in the Martian ionosphere by the Mars Global Surveyor radio science experiment, *J. Geophys. Res.*, *113*, A12314, doi:10.1029/2008JA013636.

Yagi, M., F. Leblanc, J. Y. Chaufray, F. Gonzalez-Galindo, S. Hess, and R. Modolo (2012), Mars exospheric thermal and non-thermal components: Seasonal and local variations, *Icarus*, *221*, 682–693.

©2014. American Geophysical Union. All Rights Reserved.